metals

MDPI

Article

Experimental and Numerical Simulations of the Solidification Process in Continuous Casting of Slab

Liang Bai, Bo Wang *, Honggang Zhong *, Jie Ni, Qijie Zhai and Jieyu Zhang

State Key Laboratory of Advanced Special Steel, Shanghai University, Shanghai 200072, China; bailiang410@163.com (L.B.); njpanda@163.com (J.N.); qjzhai@shu.edu.cn (Q.Z.); zjy6162@staff.shu.edu.cn (J.Z.)

* Correspondence: bowang@shu.edu.cn (B.W.); hgzhong@shu.edu.cn (H.Z.); Tel./Fax: +86-021-5633-7547 (B.W.); Tel.: +86-021-5633-4042 (H.Z.)

Academic Editor: Hugo F. Lopez

Received: 23 December 2015; Accepted: 23 February 2016; Published: 4 March 2016

Abstract: Thermal simulation equipment (TSE) was recently developed to simulate the solidification process in the industrial continuous casting of slab. The grain growth, solid-liquid interface movement, and columnar-to-equiaxed transition (CET) in the continuous casting process can be reproduced using this equipment. The current study is focused on the effects of different cooling rates and superheat conditions on the grain growth in the solidification process of chromium-saving ferritic stainless steel (B425). The temperature distribution and microstructure evolution are simulated by a Cellular Automaton-Finite Element (CAFE) model. The experimental results demonstrate that the temperature gradient and the grain growth rate of the sample can be effectively controlled by the equipment. It is observed from optical micrographs of the microstructure that the average equiaxed grain ratio increases when the superheat temperature decreases. The average equiaxed grain ratio is approximately 26% and 42% under superheat conditions of 40 °C and 30 °C, respectively, and no apparent columnar grain generation in the samples occurs under superheat conditions of 10 °C and 20 °C, as the result of a large thermal resistance at the copper-sample interface and low superheat inside the sample. A lower cooling rate results in a higher equiaxed crystal ratio in the sample. As the cooling rate decreases, the equiaxed crystal ratio becomes 14%, 23%, and 42%. Comparing the simulation results with the experimental observations, a reasonable qualitative agreement is achieved for the chilled layer thickness, grain morphology, and CET in the sample. Thus, the CAFE model in the current study can accurately predict the grain growth under different superheating and cooling rate conditions.

Keywords: thermal experimental device; numerical simulation; grain growth; CAFE model

1. Introduction

High temperature, opacity and difficult control are the characteristics of metal solidification processes. The solidification process is always accompanied by a continuous industrial production. Therefore, it is difficult to investigate the solidification process for large castings.

An industrial experiment that collects the data directly from the industrial process could directly reflect the variation in conditions during the production process. It is the most effective guide for optimizing manufacturing techniques and improving the quality of castings. However, high temperature and continuous production are the primary difficulties when collecting data. A small amount of data can be obtained from molten metal. Furthermore, industrial experiment costs are significant, thus posing considerable challenges and risks for operation. Additionally, under continuous production conditions, the general experimental methods used in metal solidification investigation, such as the pouring out method [1], quenching method [2,3], and *in-situ* observation method [4–8], cannot be performed.

Over the last several decades, metallurgical technicians have used a considerable amount of labor and financial resources to obtain technological information during the solidification of a continuous casting strand. They have designed several modeling experimental types of equipment (such as a scaled-down continuous caster) to study the continuous casting process in lower solidus temperature alloys instead of steel [9,10]. These experiments have enabled certain solidification information on the continuous casting of steel to be obtained; however, due to the difference between the characteristics of low solidus temperature alloy and steel as well as the different size and manufacturing technique processes between the experimental equipment and the industrial continuous caster, the process parameters of industrial continuous casting have been difficult to obtain. Furthermore, the cost of designing equipment and experimental processes is considerable.

Currently, Zhai [11] has designed a Thermal Simulation Equipment (TSE), which is based on characteristics similar to that of the heat transfer and grain growth characteristics in a continuous casting slab. Additionally, the primary heat of the continuous casting of slab is removed in the thickness and width directions. Furthermore, the heat transfer in the vertical direction is insignificant. The broad face of the slab is significantly larger than the narrow face. Therefore, the heat transfer rate of the broad face dominates the heat transfer in the slab. The heat transfer can be considered to be one-dimensional in most parts of the slab's cross section. The solidification process of the continuous casting slab is similar to directional solidification. Nonetheless, the differences between slab solidification and directional solidification are that the growth speed of the slab thickness is nonlinear, and the temperature gradient front of the solid-liquid interface is varied. Therefore, by controlling the temperature and the growth speed, TSE can be used to reproduce grain growth during the solidification process in the continuous casting of slab to study the grain morphology variation, solute distribution, columnar-to-equiaxed transition (CET) transformation, and effects of the technological parameters on the microstructure growth during the solidification process in the continuous casting of slab.

Compared with industrial and modeling experiments, this thermal simulation method has more advantages, such as simple operation, easily changeable cooling condition and low cost. This equipment can be used to optimize the cooling conditions and technology parameters in the continuous casting process to improve the quality of the product. Furthermore, by combining the advantages of the numerical and experimental simulations, the results of the experiment can accurately predict the industrial production process under laboratory conditions.

In this report, TSE was used to study the grain growth under different superheating and cooling rates in the continuous casting slab. The commercial software ProCAST (2009, ESI, Paris, France) was used to simulate the grain growth under experimental conditions. The nucleation and growth parameters of a CA model were validated by the TSE results; thus, the CA model can accurately describe the grain growth process in the continuous casting of slab.

2. Experimental

2.1. TSE

The schematic diagram of the TSE is illustrated in Figure 1, and the magnification of the furnace is depicted in Figure 2. The shape and size of the crucible are provided in Figure 3. The vacuum furnace is divided into a high- (Z1) and low-temperature (Z2) zone (red and light yellow zone in Figure 2, respectively) by the insulator plate. A hole was drilled into the insulator plate large enough for the sample to pass through. Before the experiment began, the furnace was moved to location one (in Figure 1), and the crucible, which is positioned on the water-cooled copper support rod, was located to the left of the insulator plate, heated to a target temperature at Z1, and held for 10 min; then, the crucible was placed upside down to complete the pouring process. Liquid metal was poured into the square from the curved sections. Furthermore, the molten metal contacts the water-cooled copper sidewall. A chilled layer is rapidly formed on the surface of the sample, and horizontal

solidification occurs. The equipment keeps the sample stationary, and the driving motor moves the furnace backwards until solidification is complete. The role of the two-stage heating source is to generate a reasonable temperature gradient in the sample, and the insulator plate is located in the solid-liquid interface. The temperature gradient should ensure that the solid-liquid interface moves with the insulator plate at the same velocity.

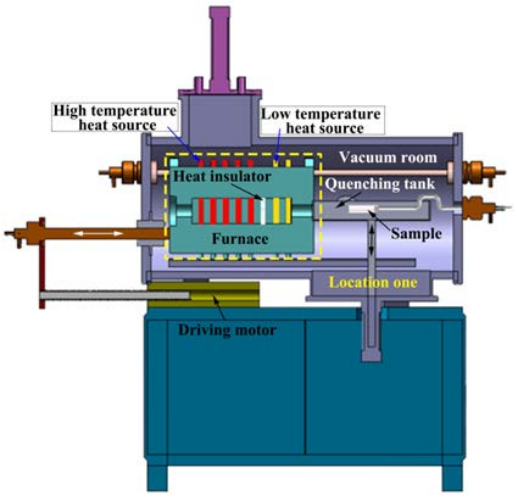

Figure 1. Schematic of the thermal simulation equipment (TSE).

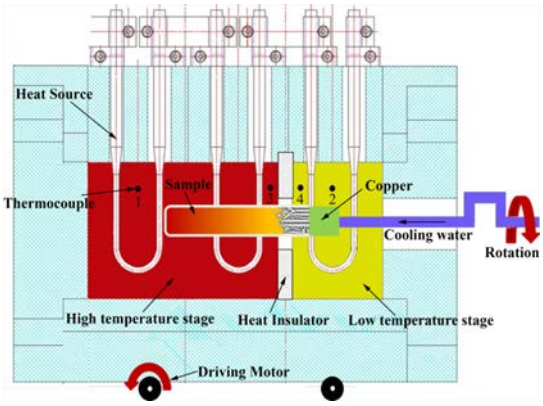

Figure 2. Magnification of the furnace.

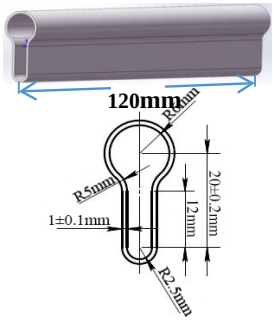

Figure 3. Size of sample and crucible.

To ensure that the temperature field and grain growth in the sample are consistent with the continuous casting slab, the temperature of the heat sources and the movement speed of the furnace need to be controlled by the temperature distribution at the core of the slab along with the casting

direction and the shell thickness growth speed of the slab. However, the temperature at the core of the slab and the shell thickness growth speed are difficult to obtain from the industrial continuous casting process. Therefore, these control parameters need to be obtained from the numerical simulation of the temperature field in the slab. The numerical model is a two-dimensional slice model, which was first applied by Samarasekera and Brimacombe [12] in 1982 and extensively developed by Thomas [13–16]. The parameters of the industrial continuous caster are listed in Table 1.

Table 1. Parameters of the continuous caster.

Parameter	Value	Parameter	Value
Casting Speed	0.8 m/min	Working mold length	0.8 m
Slab geometry, $W \times N$	200 × 600 m	Secondary cooling length	13.6 m
Superheat	20 °C	-	-

The temperature control curves and the movement speed of the furnace are illustrated in Figures 4 and 5 respectively. The experiments were conducted with four different superheating temperatures, 10 °C, 20 °C, 30 °C, and 40 °C, and three different cooling condition rates. The temperature curves of the high-temperature heat source are depicted in Figure 4. The temperature of the low-temperature heat source is 110 °C lower than the liquidus temperature, which can generate a reasonable temperature gradient in the sample. This phenomenon has been proven several times in pre-experiments. The velocity of the furnace is depicted in Figure 5, where high, mid, and low denote the cooling rates of the slab.

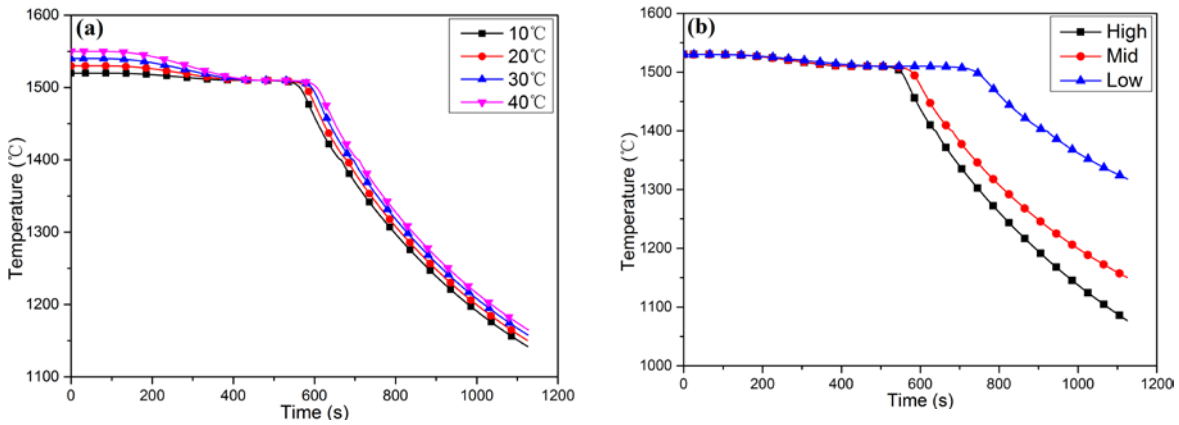

Figure 4. Temperature control curves of the high temperature heat source. (**a**) Different superheat conditions; and (**b**) different cooling rates.

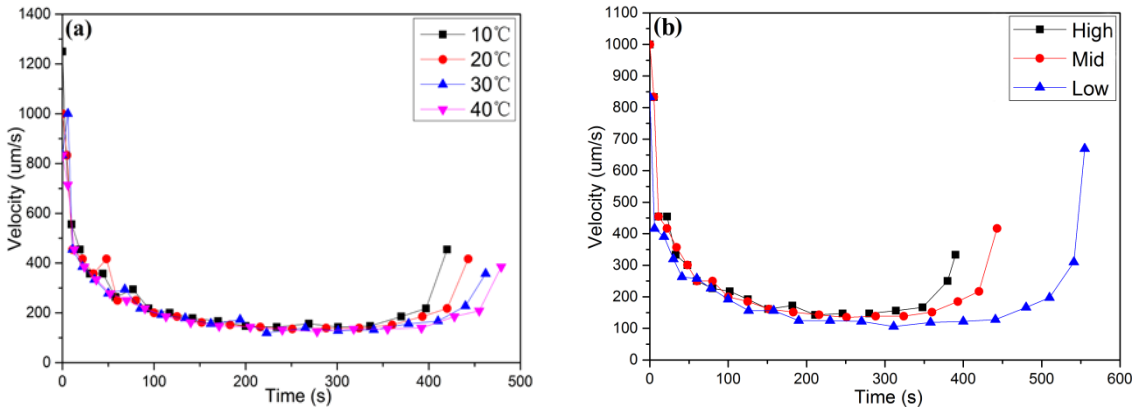

Figure 5. Velocity of the furnace. (**a**) Different superheat conditions; and (**b**) different cooling rates.

2.2. Material

The chromium-saving ferritic stainless steel B425 was designed recently by Bao Steel and has not been broadly applied in the market thus far. Compared with 430 stainless steel, B425 has more advantages, such as better processing performance and corrosion resistance, lower chromium content, and lower cost of production. Furthermore, the solidification process in the continuous casting is one of the key factors that control the quality of the strand. However, the solidification process of B425 in continuous casting is not clear. Therefore, this study process could help better understand the continuous casting solidification process in this new type of steel and guide the optimization process for the cooling conditions and technical parameters used to improve the slab quality. The chemical component of B425 was measured by ICP (LEEMAN, Hudson, NH, USA), and set out in Table 2 and the physical parameters are shown in Table 3.

Table 2. Chemical component of B425 (wt. %).

Elements	Cr	C	N	Mn	Si	P	S
Content	14.5	0.025	0.015	0.3	0.3	0.02	0.001

Table 3. Physical properties of B425.

Temperature (K)	Fraction Solid (wt. %)	Thermal Conductivity ($W \cdot m^{-1} \cdot K^{-1}$)	Specific Heat ($J \cdot g^{-1} \cdot K^{-1}$)
1783	0.043	32.7	9.02
1781	0.37	33.3	26.8
1778	0.62	33.8	12.9
1776	0.72	33.9	8.87
1773	0.82	34.1	5.64
1771	0.86	34.2	4.40
1768	0.91	34.2	3.22
1766	0.94	34.3	2.70
1763	0.97	34.3	2.16
1761	1.0	34.3	1.89

3. Model Theory

A Cellular Automaton-Finite Element (CAFE) model was used to simulate the grain growth process of the sample at the same boundary condition as the experimental equipment. The simulation of nucleation and the growth of grains are built on the macroscopic temperature field. The temperature field provided vital undercooling data for the micro simulation in the solidification process. The nucleation model is based on the continuous nucleation theory proposed by Rappaz [17,18]. The CA algorithm, which applies to non-uniform temperature cases, is fully coupled to an enthalpy-based Finite Element (FE) heat flow calculation. During each time-step, the temperature in the cell locations is interpolated from those at the FE nodal points to calculate the nucleation and the growth of grains. The nucleation process is probability density distribution dependent on the undercooling, and Gaussian distributions have been used to treat the nucleation rate and the nucleation substrates. The term $dn/d\Delta T$ is used to describe the grain density increase, dn, which is induced by an increase in the undercooling, $d\Delta T$. Therefore, the total density of the grains, $n(\Delta T)$, which have been nucleated at a given undercooling, ΔT, can be described as follows:

$$n(\Delta T) = \int_0^{\Delta T} \frac{dn}{d(\Delta T)} d(\Delta T) \quad (1)$$

$$\frac{dn}{d(\Delta T)} = \frac{n_{max}}{\sqrt{2\pi}\Delta T_\sigma} \exp\left[-\frac{(\Delta T - \Delta T_{max})^2}{2\Delta T_\sigma^2}\right] \quad (2)$$

where, n_{max}, ΔT_{max}, and ΔT_{σ} are the maximum density of the crystal nucleus, mean undercooling of the nucleation and standard deviation (the width of the Gaussian curve) at the surface and in the bulk liquid, respectively.

The KGT model, which is based on a dendrite tip solute balance, was proposed by Kurz, *et al.* [19]. In the actual simulation process, to accelerate the computation course, the KGT model is fitted, and the equation can be obtained as follows:

$$v = \alpha_2 \Delta T^2 + \alpha_3 \Delta T^3 \tag{3}$$

where ΔT is the total undercooling of the grain tip; and α_2 and α_3 are the coefficients of the multinomial of the grain growth velocity.

$$\alpha_2 = \left[\frac{-\rho}{2\,(m \cdot c_0)\,(1-k)^2 \cdot \Gamma \cdot k} + \frac{1}{(m \cdot c_0)\,(1-k) \cdot D} \right] \frac{D^2}{\pi^2 \Gamma} \tag{4}$$

$$\alpha_3 = \frac{D}{\pi \Gamma} \cdot \frac{1}{(m \cdot c_0)^2\,(1-k)} \tag{5}$$

where ρ is density of steel, kg/m^3; m is the liquidus slope, K/wt. %; D is the liquid solute diffusivity, m^2/s; and k, Γ and c_0 is the solute equilibrium partition coefficient, Gibbs-Thompson coefficient and alloy element initial concentration, respectively. In this report, the pseudo-binary alloy phase diagram method is applied to address the B425, and this alloy is split into seven Fe-X binary alloy systems, which are Fe-Cr, Fe-C, Fe-N, Fe-Mn, Fe-Si, Fe-P, and Fe-S. The composition c_0, partition coefficient k, liquidus slope m, and solute diffusion coefficient D_l of the Fe-X alloys are listed in Table 4.

Table 4. Calculation parameters for α_2 and α_3 [20–22].

Element	c_0/wt. %	m/K	k	D_l/(m$^2\cdot$ s^{-1})
Cr	14.5	−7.4	0.99	1.8×10^{-9}
C	0.025	−58	0.17	2.3×10^{-9}
N	0.015	−4.6	0.78	3.0×10^{-9}
Mn	0.3	−5.0	0.68	7.6×10^{-9}
Si	0.3	−18.7	0.65	8.5×10^{-9}
P	0.02	−48.3	0.13	4.6×10^{-9}
S	0.001	−18.7	0.65	3.5×10^{-9}

The calculated value of the liquidus temperature and the solidus temperature of B425 is T_l = 1783 K and T_S = 1758 K, respectively. The Gibbs-Thompson coefficient is Γ = 3.2×10^{-7} m·K. The nucleation parameters and growth parameters are listed in Table 5.

Table 5. Nucleation parameters and growth parameters.

Nucleation Parameter	ΔT_{max}	ΔT_{σ}	n_{max}
Surface nucleation	1.0 °C	2.0 °C	4.68×10^9 m^{-2}
Volume nucleation	1.85 °C	1.9 °C	2.82×10^8 m^{-3}
Growth parameter a_2	9.403×10^{-6} ms$^{-1}\cdot$°C^{-2}		
Growth parameter a_3	9.480×10^{-6} ms$^{-1}\cdot$°C^{-3}		

4. Results and Discussion

4.1. Grain Morphology of the Slab

The industrial continuous casting slab was cut from the center of the wide face, polished using a grinding machine, and etched. The etching solution, $V(HNO_3)$:$V(HCI)$:$V(HF)$:$V(H_2O)$ = 2.5:1.5:1:95, was used to etch the grain boundary, and the metallographic images were observed using a Canon 1500D camera (Canon, Tokyo, Japan). The macrostructure of half of the slab is depicted in Figure 6. In the figures, the yellow dashed line denotes the CET location. The average length of the columnar grain is approximately 69 mm in the slab, and the equiaxial crystal ratio is approximately 31%.

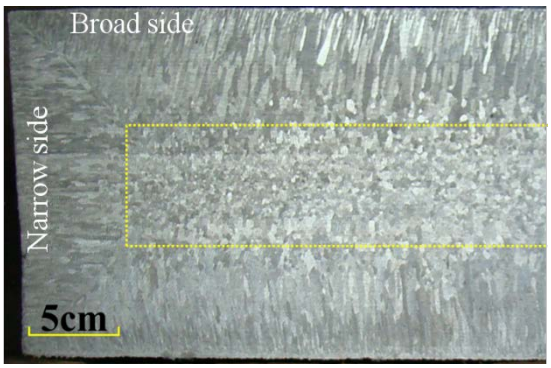

Figure 6. Macrostructure of the B425 continuous casting slab (Provided by Bao Steel).

4.2. Temperature Distribution in the Furnace

Figure 2 illustrates the locations of the thermocouples in the furnace, which are marked by the numbers 1 to 4. The temperature distribution in the furnace was monitored by these thermocouples. Thermocouples 1 and 2 are used to measure the heat sources at both sides of the heat insulator plate. Thermocouples 3 and 4 are used to record the temperature near the heat insulator plate. For example, the experimental temperature distribution under the superheat temperature of 40 °C is depicted in Figure 7.

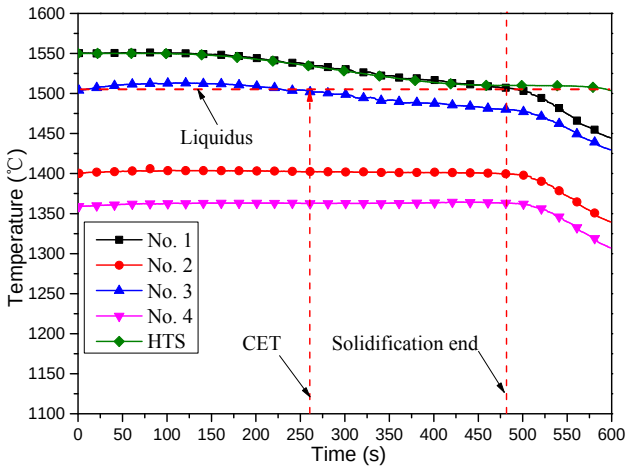

Figure 7. Temperature distribution of the furnace.

The HTS is the temperature control curve of the high-temperature heat source. Figure 7 demonstrates that the sample takes 482 s to complete the solidification process. The temperature control curve matches well with the measurement data of the high-temperature heat source before 482 s. After 482 s, the sample is pulled out of the furnace, and the power for the heat source is shut off.

The furnace is cooled by natural cooling to room temperature. Thus, the temperature curve does not match between No. 1 and HTS. Furthermore, the low-temperature heat source is accurately controlled at 1400 °C below the liquidus of 110 °C. This result proves that the temperature of the furnace was perfectly controlled through pre-setting during the experimental process. The No. 3 curve indicates a temperature change near the left side of the heat insulator plate. The temperature climbed above the liquidus temperature before 262 s. Then, the temperature decreased into the mush zone, and this temperature curve was parallel with the No.1 curve. This result guarantees a stable temperature gradient in the sample due to the furnace moving backwards. The CET location in the sample is performed from 262 s, and the temperature of the solid-liquid interface below the liquidus causes the equiaxed grains to start to nucleate.

4.3. Grain Growth

Based on the above control parameters, the solidification process of the sample was conducted by TSE. Figure 8 depicts the macrostructure morphology changes under the different cooling rates. For easy metallographical processing, the samples were cut from the middle (at approximately 5 cm). After taking photographs, the two images were joined together. The equiaxed grain ratio of the figures was measured using an Image-Pro Plus 6.0 (MEDIA CYBERNETICS, Bethesda, MD, USA). The grain morphology of the slab was simulated by TSE under the same cooling conditions and superheat temperatures. The result is illustrated in Figure 8b.

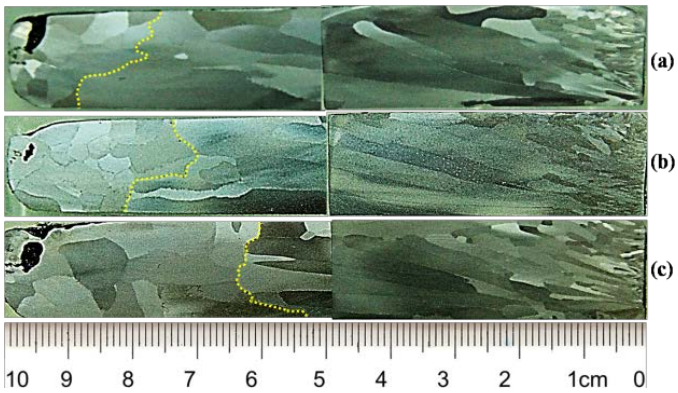

Figure 8. Macrostructural changes under different cooling conditions. (**a**) High cooling rate; (**b**) middle cooling rate; and (**c**) low cooling rate.

In Figure 8b, the length of the columnar grain is approximately 73 mm, and the equiaxial crystal ratio is approximately 23%. The relative error of the columnar grain between the sample and the slab is 8%, and the size of the grain is slightly larger than the grain size of the slab. However, the thickness of the chilled layer, grain morphology, and equiaxial grain generation of the sample agreed well with the industrial slab.

It can be seen that a chilled layer of approximately 2–3 mm in thickness was generated near the copper surface. Additionally, the thickness of the chilled layer did not change significantly with a change in the control parameter. The foremost reason is that the chilled layer is rapidly generated when pouring is complete. A tiny gap was generated between the chilled layer and the copper surface due to solidification shrinkage, and the cooling conditions were changed. Therefore, the thickness of the chilled layer is no longer sensitive to the cooling rate, and the thickness will not increase with an increase in the cooling rate. The CET is gradually brought forward as the cooling rate decreases. The equiaxed crystal ratio was 14%, 23%, and 42% under high, medium, and low cooling rates, respectively.

To consider the influence of the slag and the Cr/Ni coating at the mold surface on the cooling rate, the interface between the sample and the copper was coated with a thin layer of zirconia. The influence

of superheat on the grain growth is depicted in Figure 9. The columnar grains only generated under 30 °C and 40 °C, and the columnar grain increased with an increase in the superheat temperature. The average equiaxed grain rate is approximately 26% and 42% for a superheat temperature of 40 °C and 30 °C, respectively. Additionally, there is no apparent columnar grain generation in the samples at the superheat temperatures of 10 °C and 20 °C, caused by a large thermal resistance at the copper-sample interface and a low superheat inside the sample. The morphology of the grains depends on the G/R ratio, where G and R are the temperature gradient and the solidification rate, respectively [23]. A low G/R ratio is beneficial for the formation of equiaxed grains. When the chilled layer is generated, the thermal resistance between the sample and the water-cooled copper is further increased. As the solidification layer increases, the temperature gradient decreases from the surface to the inside of the sample, thus resulting in a low G/R ratio. Thus, the CET transformation is performed early in the samples under the superheat temperatures of 10 °C and 20 °C. Furthermore, the CET occurred at 65 mm and 75 mm under the superheat temperatures of 30 °C and 40 °C, respectively.

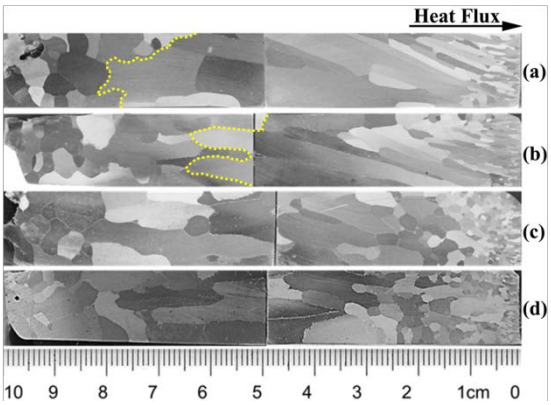

Figure 9. Influence of superheat on grain growth. (**a**) 40 °C; (**b**) 30 °C; (**c**) 20 °C; and (**d**) 10 °C.

Additionally, the experimental results indicated that the columnar crystal has a tendency to grow to the top surface of the sample. This phenomenon is due to the temperature difference along the vertical direction of the sample. After pouring, the top surface of the sample does not contact the crucible, and the heat transfer by convection and thermal radiation is smaller than that in the other area, where the sample and crucible are in close contact. Therefore, the temperature at the top is higher than that at the bottom of the sample. The columnar grain follows the heat flux direction and grows to the top surface of the sample.

Figures 8b and 9c are performed at constant superheat conditions and cooling rates. The only difference is that the copper surface is coated with the zirconia layer in Figure 9c. Additionally, G is the driving force of the columnar grain growth. In Figure 9c, G is considerably lower than that of the sample without coating; thus, only a 3 mm long columnar grain was generated. The sample without coating generates a large temperature gradient at the front of the chilled layer. R is further increased, but it is limited by the furnace movement speed. Thus, the columnar grain continuously grows until the G/R ratio becomes lower than the critical value. A higher intensity at the cooling surface of the sample generates a longer columnar grain in the chilled layer and inside the sample.

4.4. Numerical Simulation Results

The solidified structure of the samples depends critically on the temperature distribution and fluid motion in the molten region. In ProCAST, the TILT method was developed to handle the undesired "sticking" in the pouring cup during tilt pouring. Here, TILT is used to reproduce the tilt pouring process in the crucible. Furthermore, the boundary of the sample is identical to the control parameters

of the heat sources and the furnace movement velocity. The simulation result due to the influence of superheat on the grain growth is depicted in Figure 10.

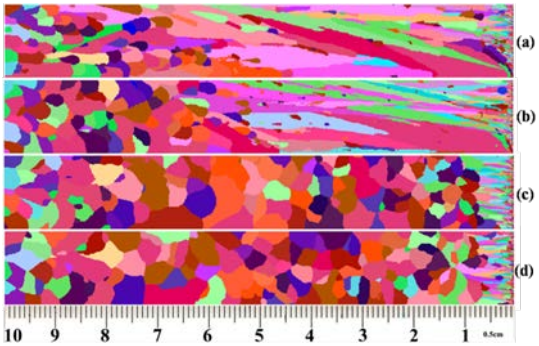

Figure 10. Numerical simulation result of the grain growth with different superheat conditions. (**a**) 40 °C; (**b**) 30 °C; (**c**) 20 °C; and (**d**) 10 °C.

There are three distinct grain zones in the samples: chilled zone, columnar zone, and central equiaxed grain zone. The grain morphology transformation is significantly different when the superheat temperature decreases. The CET location occurs at 65 mm and 75 mm under superheat conditions of 30 °C and 40 °C, respectively. By comparing with the experimental and numerical simulations, it can be found that the CAFE model in the current study accurately predicted the grain morphology change and CET location in the samples under different superheat conditions.

Furthermore, it should be noted that the columnar grains grow obliquely upwards to the top of the sample in Figure 10a,b. The top surface of the sample does not contact the crucible during the simulation process; thus, the temperature at the top is higher than that at the bottom of the sample. The temperature distribution along the vertical direction of the sample is depicted in Figure 11. The 20 mm, 60 mm, and 100 mm are the distances to the cooling surface of the sample. The result indicates that the CAFE model also accurately predicted the columnar grain growth direction.

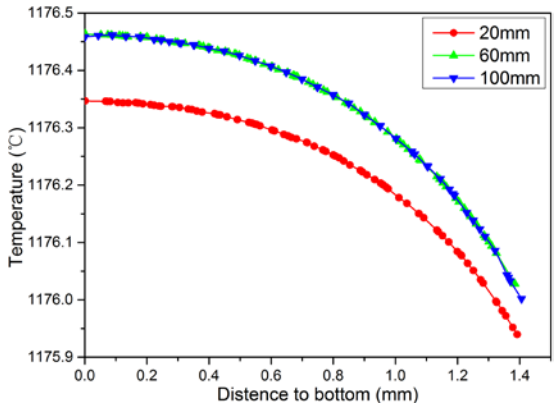

Figure 11. Numerical simulation of the temperature distribution from the top to the bottom of the sample.

The numerical simulations of the high, middle, and low cooling conditions were performed with the same nucleation and growth parameters. The results are presented in Figure 12. It can be observed that the thickness of the chilled layer did not change significantly with a decrease in the cooling intensity, and the thickness was approximately 2–3 mm. The CET is primarily controlled by the ratio of the nucleation rate and the growth rate, and is performed when the nucleation takes the dominant position. In the samples, the CET gradually moves forward with a decrease in the cooling

rate, and the equiaxed crystal ratio is 13%, 25%, and 40%. Additionally, the columnar crystal tends to grow towards the top surface of the sample for the same reason. Compared with the experimental results, the relative error of the numerical simulations for the high, middle, and low cooling rates is 7.14%, 8.7%, and 4%, respectively.

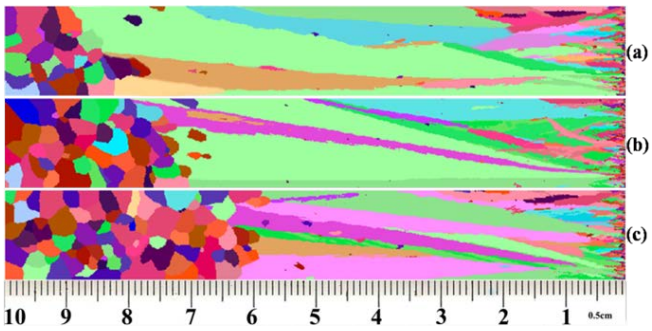

Figure 12. Grain morphology of the simulation result under different cooling conditions. (**a**) High cooling rate; (**b**) middle cooling rate; and (**c**) low cooling rate.

5. Conclusions

The grain growth process under different superheat and cooling rate conditions was investigated by experimental and numerical simulations. The results indicate that the columnar grain is only generated under superheat conditions of 30 °C and 40 °C, and the columnar grain grows longer as the superheat temperatures increase. The average length of the columnar grain is approximately 74 mm and 58 mm at the superheat conditions of 40 °C and 30 °C, respectively. There is no columnar grain generation in the samples at the superheat conditions of 10 °C and 20 °C, caused by the lower cooling intensity at the surface of the sample and the temperature gradient inside of the sample. Without the coating on the copper surface, the CET gradually moves forward, and the equiaxed crystal ratio increases from 14% to 42% with a decrease in cooling rate.

By comparing the experimental results with the numerical simulations, it can be determined that the CAFE model in the current study can accurately predict the thickness of the chilled layer, grain morphology change, and CET location in the samples under different superheat and cooling rate conditions. The relative error of the numerical simulation for the equiaxed crystal ratio under the high, middle, and low cooling rates is 7.14%, 8.7%, and 4%, respectively. Thus, the model can provide guidance for the optimization of TSE.

Acknowledgments: The authors gratefully acknowledge financial support from the National Natural Science Foundation of China (No. 51227803 and No. 51474143), National Key Technology R & D Program of China (No. 2012BAE04B02) and Shanghai Economic and Information Commission (No. Hu CXY-2013-1).

Author Contributions: Honggang Zhong and Qijie Zhai conceived and designed the equipment and experiments; Bo Wang and Jieyu Zhang contributed the numerical simulation; Jie Ni performed the experiments; and Liang Bai analyzed the data and wrote the report.

Conflicts of Interest: The authors declare no conflict of interest.

References

1. Fredriksson, H.; Hillert, M. On the formation of the central equiaxed zone in ingots. *Metall. Mater. Trans. B* **1972**, *3*, 569–574. [CrossRef]
2. Burden, M.H.; Hunt, J.D. Cellular and dendritic growth II. *J. Cryst. Growth* **1974**, *22*, 109–116. [CrossRef]
3. Burden, M.H.; Hunt, J.D. Cellular and dendritic growth I. *J. Cryst. Growth* **1974**, *22*, 99–108. [CrossRef]
4. Wang, T.M.; Xu, J.J.; Li, J.; Huang, W.X.; Liu, S.C.; Li, T.J. *In situ* study on dendrite growth of metallic alloy by a synchrotron radiation imaging technology. *Sci. China Technol. Sci.* **2010**, *53*, 1278–1284. [CrossRef]

5. Ruvalcaba, D.; Mathiesen, R.H.; Eskin, D.G.; Arnberg, L.; Katgerman, L. *In situ* observations of dendritic fragmentation due to local solute-enrichment during directional solidification of an aluminum alloy. *Acta Mater.* **2007**, *55*, 4287–4292. [CrossRef]
6. Arnberg, L.; Mathiesen, R.H. The real-time, high-resolution X-ray, video microscopy of solidification in aluminum alloys. *JOM* **2007**, *59*, 20–26. [CrossRef]
7. Mathiesen, R.H.; Arnberg, L.; Bleuet, P.; Somogyi, A. Crystal fragmentation and columnar-to-equiaxed transitions in Al-Cu studied by synchrotron X-ray video microscopy. *Metall. Mater. Trans. A Phys. Metall. Mater. Sci.* **2006**, *37A*, 2515–2524. [CrossRef]
8. Junichi, C.; Fujimoto, I.; Asaeda, Y. X-ray topography with chromatic-aberration correction. *J. Appl. Phys.* **1971**, *42*, 4731–4735.
9. Lei, Z.S.; Zhang, B.W.; Deng, K.; Ren, Z.M. Study on Meniscus Temperature Fluctuation during Mold oscillation in Continuous Casting by Modeling Experiments. *J. Shanghai Univ.* **2002**, *6*, 236–239. [CrossRef]
10. Mahapatra, R.B.; Brimacombe, J.K.; Samarasekera, I.V. Mold behavior and influence on quality in the continuous casting of steel slabs. Part II. Mold heat transfer, mold flux behavior formation of oscillation marks, longitudinal off-corner depressions, and subsurface cracks. *Metall. Trans. B* **1991**, *22*, 861–888. [CrossRef]
11. Zhang, C.; Ye, J.Z.; Wu, C.S.; Hu, J.C.; Zhong, H.G.; Zhai, Q.J. The effect of cooling intensity on the solidification structure and ferrite phase fraction of a duplex stainless steel. In Proceedings of EPD Congress 2014, San Diego, CA, USA, 16–20 February 2014; pp. 463–470.
12. Samarasekera, I.V.; Brimacombe, J.K. Thermal and Mechanical Behavior of Continous-casting Billet Molds. *Ironmak. Steelmak.* **1982**, *9*, 1–15.
13. Thomas, B.G.; Samarasekera, I.V.; Brimacombe, J.K. Comparison of numerical modeling techniques for complex, two-dimensional, transient heat-conduction problems. *Metall. Trans. B* **1984**, *15B*, 307–318. [CrossRef]
14. Thomas, B.G. *Mathematical Models of Continuous Casting of Steel Slabs, Annual Report to Continuous Casting Consortium*; UIUC: Champaign, IL, USA, 1995.
15. Thomas, B.G.; Ho, B.; Li, G. *CON1D V. 3.1 User Manual*; Report to Continuous Casting Consortium: Urbana, IL, USA; 14 January 1995.
16. Meng, Y.; Thomas, B.G. Heat-transfer and solidification model of continuous slab casting: CON1D. *Metall. Mater. Trans. B* **2003**, *34B*, 658–705. [CrossRef]
17. Rappaz, M.; Gandin, C.A. Probabilistic modelling of microstructure formation in solidification processes. *Acta Metall. Mater.* **1993**, *41*, 345–360. [CrossRef]
18. Gandin, C.A.; Rappaz, M. A coupled finite element-cellular automaton model for the prediction of dendritic grain structures in solidification processes. *Acta Metall. Mater.* **1994**, *42*, 2233–2246. [CrossRef]
19. Kurz, W.; Giovanola, W.; Trivedi, R. Theory of microstructural development during rapid solidification. *Acta Metall.* **1986**, *34*, 823–830. [CrossRef]
20. Yu, J.Q.; Yi, W.Z.; Chen, B.D. *Binary Alloy. Phase Diagram (in Chinese)*; Shanghai Scientific and Technical Publishers: Shanghai, China, 1987.
21. Chen, J.X. *Ferrous Metallurgy (in Chinese)*; Metallurgical Industry Press: Beijing, China, 2004.
22. Li, W.C. *Physical Chemistry of Metallurgy and Material (in Chinese)*; Metallurgical Industry Press: Beijing, China, 2001.
23. McLean, M. *Directly Solidified Materials for High Temperature Service*; The Metals Society: London, UK, 1983.